Biosensors and Bioelectronics 107 (2018) 224–229

Contents lists available at ScienceDirect

Biosensors and Bioelectronics

journal homepage: www.elsevier.com/locate/bios

An optofluidic metasurface for lateral flow-through detection of breast cancer biomarker

Yifei Wang[a], Md. Azahar Ali[a], Edmond K.C. Chow[b], Liang Dong[a,c,*], Meng Lu[a,c,d,*]

[a] Department of Electrical and Computer Engineering, Iowa State University, Ames, IA 50011, USA
[b] Micro and Nanotechnology Laboratory, University of Illinois at Urbana-Champaign, Urbana, IL 61801, USA
[c] Microelectronics Research Centre, Iowa State University, Ames, IA 50011, USA
[d] Department of Mechanical Engineering, Iowa State University, Ames, IA 50011, USA

ARTICLE INFO

Keywords:
Optofluidics
Metasurface
Flow-through biosensor
Breast cancer biomarker

ABSTRACT

The rapid growth of point-of-care tests demands for biosensors with high sensitivity and small size. This paper demonstrates an optofluidic metasurface that combines silicon-on-insulator (SOI) nanophotonics and nanofluidics to realize a high-performance, lateral flow-through biosensor. The metasurface is made of a periodic array of silicon nanoposts on an SOI substrate, and functionalized with specific receptor molecules. Bonding of a polydimethylsiloxane slab directly onto the surface results in an ultracompact biosensor, where analyte solutions are restricted to flow only in the space between the nanoposts. No flow exists above the nanoposts. This sensor design overcomes the issue with diffusion-limited detection of many other biosensors. The lateral flow-through feature, in conjunction with high-Q resonance modes associated with optical bound states of the metasurface, offers an improved sensitivity to subtle molecule-bonding induced changes in refractive index. The device exhibits a resonance mode around 1550 nm wavelength and provides an index sensitivity of 720 nm/RIU. Biosensing is conducted to detect the epidermal growth factor receptor 2 (*ErbB2*), a protein biomarker for early-stage breast cancer screening, by monitoring resonance wavelength shifts in response to specific analyte-ligand binding events at the metasurface. The limit of detection of the device is 0.7 ng mL^{-1} for *ErbB2*.

1. Introduction

Optical label-free biosensors can detect biomolecules based on their intrinsic physical properties, such as Raman scattering, refractive index, and second harmonic generation (Celebrano et al., 2015; Choi et al., 2010b; Salafsky, 2006; Wu et al., 2012). In particular, many refractive index-based biosensors have been implemented to study analyte-ligand interactions without using labels (Im et al., 2014; Liu et al., 2014; Zhang et al., 2008). In contrast to binding assays that require fluorescent or enzymatic tags, label-free assays often eliminate the need for time-consuming labeling processes and can monitor binding kinetics in real time (Ali et al., 2015; Ali et al., 2017b; Diaz-Diestra et al., 2017). Therefore, label-free biosensors are gaining increasing attention in the fields of life sciences, pharmaceutics, and clinic diagnosis (Bergwerff and Van Knapen, 2006; de Mol, 2012; Fivash et al., 1998; McDonnell, 2001; Navratilova and Hopkins, 2011; Rich and Myszka, 2003; Sridharamurthy et al., 2007; Thillaivinayagalingam et al., 2010; Xue et al., 2014a, 2014b). Recently, optical resonators using surface plasmon resonance, photonic crystal, and whispering gallery mode (Arnold et al., 2003; Cunningham et al., 2004; Fan et al., 2008; Heeres et al., 2009; Sun and Fan, 2011; Vollmer and Arnold, 2008) have been extensively studied and exploited for label-free biosensors. Owing to their strong ability to confine resonating fields, these biosensors are sensitive to the presence of biomaterials immobilized in the close vicinity of their surfaces (Sun et al., 2016b).

While significant progress has been made to develop optical label-free biosensors, how to efficiently delivery samples to the sensor surface remains challenging. To address the issue with the mass transfer limitation, microfluidic systems have been developed and applied to label-free biosensors (Choi and Cunningham, 2006, 2007). To improve the integration between the sensing and fluidic elements, several optofluidic biosensors (e.g., liquid-core ring resonators (White et al., 2006) and anti-resonant reflecting optical waveguides (Yin et al., 2004)) have been used to facilitate the transport of analyte. Both the microfluidic and optofluidic approaches rely on a flow-over scheme, where liquid samples flow through a channel, during which the analytes diffuse from the sample stream onto the surface of the biosensor (Brolo et al., 2004; Lindquist et al., 2009; Sinton et al., 2008; Wang et al., 2014). Recently, a vertical flow-through sensor design was implemented to label-free optical biosensing, where liquid samples flow through a horizontally

* Corresponding authors at: Department of Electrical and Computer Engineering, Iowa State University, Ames, IA 50011, USA.
E-mail addresses: ldong@iastate.edu (L. Dong), menglu@iastate.edu (M. Lu).

https://doi.org/10.1016/j.bios.2018.02.038
Received 14 December 2017; Received in revised form 12 February 2018; Accepted 14 February 2018
Available online 17 February 2018
0956-5663/

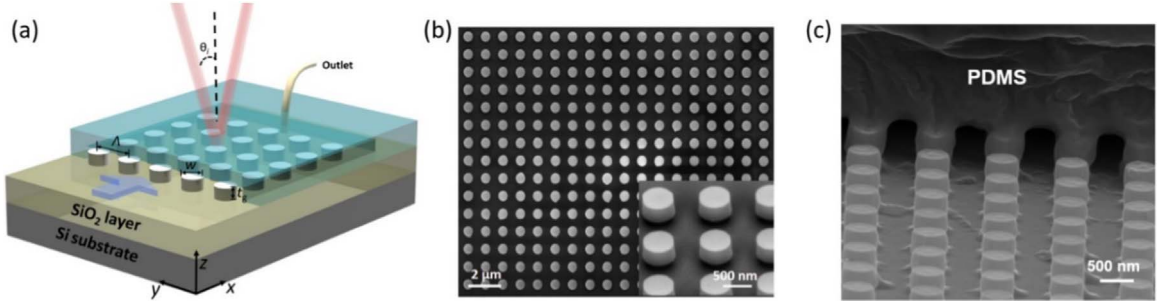

Fig. 1. (a) Schematic illustration of the optofluidic metasurface with a 2D array of SNPs. (b) SEM image of the fabricated SNPs. The inset shows a perspective view of the SNPs. (c) SEM images of the nanofluidic channel where the SNPs are sandwiched between the buried oxide of an SOI substrate and a capped PDMS cover. A sample can laterally flow through the SNP region and be captured by the recognition biomolecules onto the metasurface.

placed, nanopatterned dielectric or metallic diaphragm with nanoholes that functions as both the sensing element and conduits (Cetin et al., 2014; Eftekhari et al., 2009; Escobedo et al., 2010; Yanik et al., 2010). This sensor has enhanced the interaction between the sensing surface and analytes, thus reducing detection time.

This paper reports on a novel lateral flow-through biosensor, consisting of a metasurface with a two-dimensional (2D) periodic array of silicon nanoposts (SNPs), for the detection of cancer biomarker. The structure is manufactured in the thin top silicon layer of a silicon-on-insulator (SOI) substrate, coated with graphene oxide (GO) nanosheets, and biofunctionalized with specific antibody molecules. A polydimethylsiloxane (PDMS) slab with an inlet and an outlet is bonded to the top surface of the SNPs, thus restricting the flow of liquid analytes in between the PDMS and the buried oxide layer of the SOI substrate (Fig. 1). It is worth noting that silicon or SOI-based metasurfaces have attracted increasing attention due to the flexibility in tuning of their optical properties (Sun et al., 2016a; Zhu et al., 2015, 2013a), and the fabrication compatibility with complementary metal-oxide-semiconductor (CMOS) process. The high refractive index of silicon is favourable for light modulation (Cheung et al., 2012; Fang et al., 2016; Ferrara et al., 2015; Taillaert et al., 2006; Van Laere et al., 2007), e.g., to enhance optical fields. Our biosensor is featured with the lateral flow-through design for improved analyte-ligand interactions at the metasurface. Owing to a reduced diffusion length, the biosensor design will overcome the issue of mass transfer limit that occurs in many existing label-free biosensors (Choi et al., 2010a). Therefore, the biosensor will have an improved sensitivity and a reduced assay time. In addition, the metasurface supports different optical resonance modes, such as the bound states in the continuum (BIC) mode, and leaky waveguide mode (Chang-Hasnain and Yang, 2012; Wang et al., 2016a, 2016b), to detect biomolecule absorptions. In this work, the guided mode resonance (GMR) mode, whose linewidth depends on the coupling angle, is utilized and exhibits a high sensitivity to a change in refractive index at the surface of SNPs. The sensor design emphasizes both analyte delivery and sensitivity. The key figure of merit of the device and its ability to detect cancer biomarkers are demonstrated.

2. Experimental section

2.1. Fabrication of the optofluidic metasurface

An SOI wafer is used to fabricate the SNPs. First, 200 nm-thick PMMA is coated onto the substrate at 2000 rpm for 45 s. Subsequently, e-beam lithography is used to pattern the nanoholes array in the PMMA. Next, a 15 nm-thick Al_2O_3 layer is evaporated using electron-beam evaporation, and then patterned using lift-off process, to form a protection layer during the following deep reactive-ion etching of Si (Fig. 1(b)). After the SNPs are formed, the Al_2O_3 layer is removed via wet chemical etching. The overall size of the device is $1 \times 1\ mm^2$. To enable laterally flowing liquid analytes through the SNP area, a 2 mm-thick PDMS slab with the pre-drilled inlet and outlet is bonded directly onto the top surface of the SNPs via oxygen plasma treatment. Fig. 1(c) shows the formed nanofluidic channels embedded with the SNPs.

2.2. Setup for optical reflection measurement

A tunable laser (ANDO, AQ4321) is used as a light source providing a wavelength range from 1520 nm and 1620 nm with a central wavelength of 1570 nm. The light is collimated and incident onto the metasurface through a 50/50 beam splitter cube. The biosensor is mounted on a rotation stage to adjust the angle of incidence. The reflection spectrum is measured in real time using an InGaAs photodetector synchronized through an oscilloscope.

2.3. ErbB2 detection assay

The biosensor is used to quantify a well-established breast cancer biomarker, *ErbB2* (Ali et al., 2017a). The biofunctionalization of the surface begins with introducing an intermediate layer of GO to the surface. The GO layer allows enhancing the loading capability of *anti-ErbB2* molecules. In this step, the metasurface is treated with oxygen plasma for 50 s to make the SNPs hydrophilic. Next, a well-dispersed solution of single-layer GO nanosheets (0.4 mg/mL) is prepared in DI water, followed by thorough sonication for 1 h. 50 μL of this solution is drop-cast onto the metasurface and then dried at room temperature (25 °C) for 2 h. 20 μL of PBS (pH = 7.4) solution containing *anti-ErbB2* molecules (0.24 μM) is drop-cast onto the GO-coated metasurface, followed by treating a mixed solution of EDC (1-ethyl-3-(3-dimethylaminopropyl) carbodiimide hydrochloride, 0.2 M) and NHS (N-hydroxysuccinimide, 0.05 M) at a 1:1 ratio (Ali et al., 2016a). The abundant oxygenated groups such as –COOH and –CHO at GO are activated and utilized to make covalent binding with *anti-ErbB2* using the EDC-NHS coupling chemistry (Ali et al., 2016b, 2017a). To immobilize antibody molecules, the metasurface is kept in a humidity chamber for 12 h, and then is washed with PBS to remove unbound antibody molecules. The resulting primary amine groups present at *anti-ErbB2* bind with carboxyl groups at GO to form strong CH-NH amide bonds. Finally, 2.0 mg/mL of bovine serum albumin molecules is used to block non-specific sites of anti-*ErbB2* on the metasurface.

3. Results and discussion

3.1. Nanophotonic and nanofluidic simulations

The SNP array (350 nm thickness) is designed on the top of a 3 μm-thick oxide layer to provide an optical resonance around 1550 nm wavelength. The silicon device layer is transparent around this wavelength and has a negligible extinction coefficient $\kappa < 0.001$ and a large refractive index $n = 3.477$. The geometric parameters of the SNPs include the array period (Λ), nanopost width (w), device layer thickness

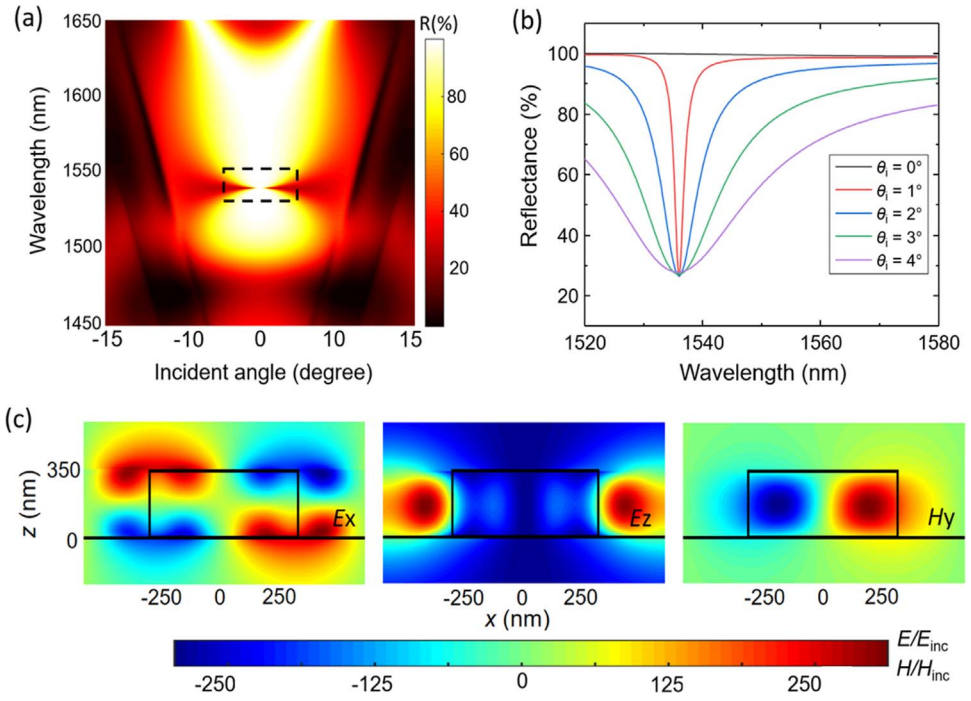

Fig. 2. Simulated optical characteristics of the 2D array of SNPs. a) Calculated reflection spectra over the wavelength range 1450–1650 nm, incident angle (θ_i) in the range of − 15 to 15°. The region indicated by the black box contains a one BIC mode appears at λ_r = 1536 nm at θi = 0. b) Calculated reflection spectra calculated for θ_i = 0°, 1°, 2°, 3°, 4°, and 5°. c) Near-field distributions of the E_x, E_z, and H_y components when λ_r = 1536 nm and θ_i = 1°.

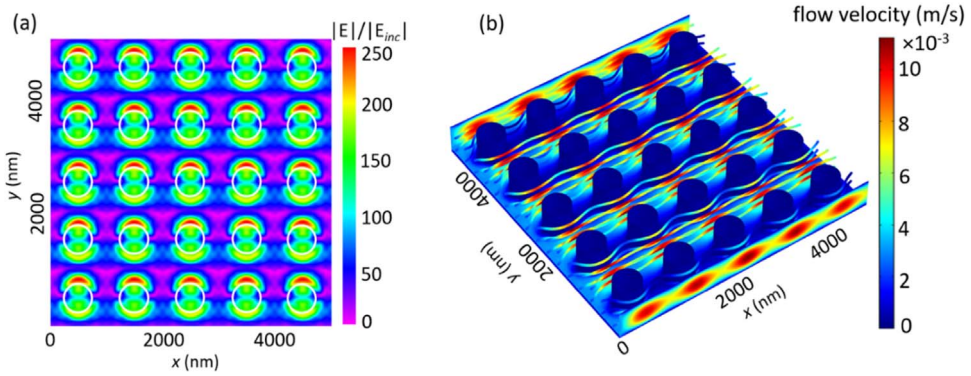

Fig. 3. (a) Calculated near-field distribution of E_x for five periods of the SNPs in the *x*-*y* plane. (b) Simulated distribution of flow rate when the liquid sample passes through the lateral flow-through biosensor.

(t_g), and duty cycle ($\eta = w/\Lambda$). The basic principle of the SNPs and corresponding optical characteristics have been discussed in our previous work (Wang et al., 2016b). The SNPs exhibit a BIC mode and a GMR mode, depending on the angle of incidence. As illustrated in Fig. 1(a), the angle of incidence is defined in terms of a standard spherical coordinate system, with the polar angle θ_i being measured from the *z*-axis. Because of the symmetry, the optical responses of the device are polarization-independent when $\theta_i = 0$.

Rigorous coupled wave analysis (RCWA) is used to study optical resonances and evaluate their performances for detecting biomolecules (Fig. 2). The details of the RCWA simulation method are described in Supplementary information. Fig. 2(a) presents the obtained photonic band diagram of the SNPs obtained by plotting the calculated reflection spectra as a function of θ_i. The wavelength and the incident angle change from 1450 nm to 1650 nm, and from − 15 to 15°, respectively. The region indicated by the black box (Fig. 2(a)) contains a BIC mode, which appears at λ_r = 1536 nm and θ_i = 0. For the angles near the BIC mode, the strong reflection regions accommodate high-sensitivity resonance features. Fig. 2(b) compares the simulated reflection spectra for θ_i = 0°, 1°, 2°, 3°, and 4°. Since the characteristics of these two modes are similar to the transverse magnetic (TM)-polarized modes of the one-dimensional grating based metasurface demonstrated previously (Wang et al., 2016b), these modes can be named TM-like resonance modes. The obtained resonant linewidth decreases as the incidence angle approaches 0°. For example, the resonance linewidth at θ_i = 4° is found to be 30 nm, corresponding to a Q-factor of 52. In comparison, the Q-factor significantly increases to 900 when θ_i is reduced to 1°. The vanishing of the linewidth at θ_i = 0° implies the existence of BIC.

The near-field distributions of the resonance mode in the *xz*-plane (Fig. 1) are calculated using the RCWA method (Fig. 2(c)). The distributions of the E_x, E_z, and H_y components are associated with the resonance (Q-factor = 900) at λ_r = 1536 nm and θ_i = 1°. The colour scale represents the amplitudes of the electric and magnetic fields normalized to the amplitude of the incident field. As seen from the field distributions, the maximum field enhancement factor is as high as 300. The enhancement factor of the field intensity is calculated by averaging the electric field intensities within the sensor area ($-\Lambda/2 < x < \Lambda/2$ and $0 < z < 350$ nm). As a result, the averaged enhancement factor of the field strength (intensity or amplitude) is $\sim 2.7 \times 10^5$. The distributions of the tangential components (E_x and H_y) appear asymmetric. The mode can be excited because of the asymmetric nature of the incident wave at θ_i = 1°. Fig. 3(a) shows the normalized near-field distribution of E_x in the *xy*-plane at the center of SNPs (z = 175 nm). The

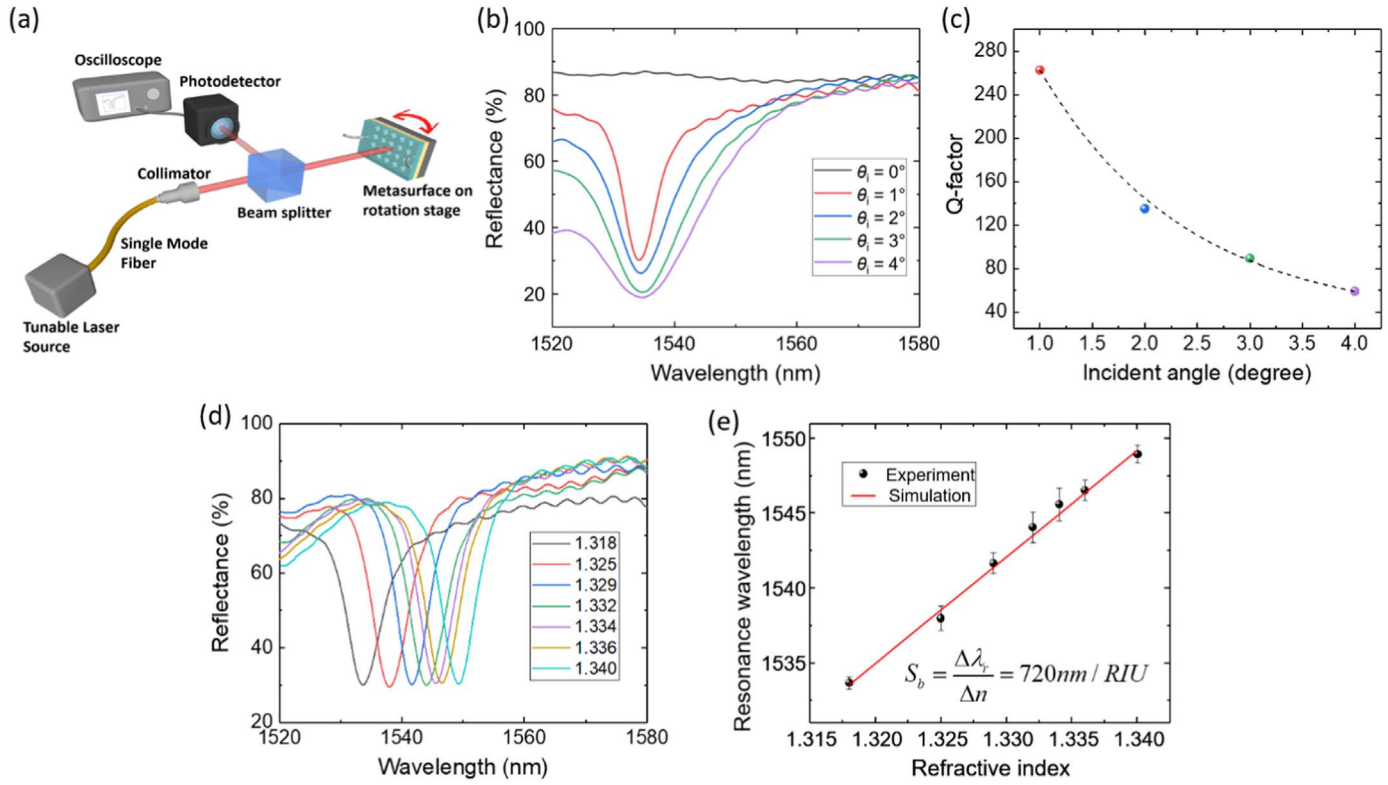

Fig. 4. (a) Schematic diagram of the reflection measurement setup (b) Measured reflection spectra of the biosensor at five different angles of incidence. (c) Q-factor of the resonances as a function of θ_i. The data is fitted to demonstrate the exponential decrease of the Q-factor when θ_i. increased from 0° to 4° (d) Reflection spectra of the device with the sample surface immersed in DI water and solutions of ethanol-water mixtures. The spectra were measured at θ_i. = 1°. (e) Simulation (red line) and experiment (black dots) results of the resonance wavelength as a function of the refractive index.

plot shows five periods of the SNPs along both the *x*- and *y*- directions.

Fluid dynamics simulations are carried out to illustrate the flowing of an aqueous sample through the SNP area (see the details in Supplementary information). Fig. 3(b) displays the flow velocity distribution at the steady state. The sample solution is infused into the channel from the inlet (left boundary) and exits from the outlet (right boundary). The analytes in the sample are not only brought to the sensor surface by the steams, but also diffuse to the sensor surface for the analyte-ligand interactions. To ensure high output signals, we chose the optical resonance, at which the localized optical field (Fig. 3(a)) well overlaps with the region of analyte absorption. As shown in the following section, the biosensor is characterized at $\theta_i = 1^\circ$ to obtain an optimized response.

3.2. Characterization of metasurface

3.2.1. Optical characterization

The fabricated metasurface was characterized by measuring the reflectance from the metasurface using the setup shown in Fig. 4(a). The reflection at a specific angle of incidence was measured in the near infrared range. A tunable laser, whose emission wavelength ranging from 1520 nm to 1620 nm, was used as the excitation. The reflected laser beam was measured using an InGaAs photodetector.

Fig. 4(b) compares the measured reflection spectra when $\theta_i = 0^\circ, 1^\circ, 2^\circ, 3^\circ$, and 4°. The black curve represents the reflectance at $\theta_i = 0^\circ$ where the BIC mode resides. Because the BIC mode is completely bound, there is no signature of resonance in the spectrum. When θ_i increases, the optical resonances appear as the narrowband dips in the reflection spectra. At $\theta_i = 1^\circ$, the BIC mode turns into a radiative resonance at $\lambda_r = 1534$ nm with a linewidth of $\delta\lambda_r = 5.8$ nm. Further increasing θ_i from 1° to 4° results in a significant increase of the resonance linewidth, while the resonance wavelength remains near $\lambda_r = 1537.2$ nm. The measured spectra agree well with the simulated results (Fig. 2(b)). To illustrate how to tune the resonance strength by changing θ_i, the Q-factor is plotted as a function of θ_i (Fig. 4(c)). The Q-factor decreases exponentially from 270 to 57 with increasing θ_i from 1° to 4°. It is worth noting that the resonance features a flat angular dispersion, which can be exploited to realize refractive index-based sensing with a focused excitation.

3.2.2. Refractometric sensing

Fig. 4(d) compares the measured reflection spectra when the metasurface is covered with different index solutions. The solutions are prepared by mixing deionized (DI) water and ethanol at different ratios of 1:2, 4:5, 1:1, 4:3, 2:1, 4:1, and 1:0, to produce the refractive indices of $n = 1.340, 1.336, 1.334, 1.332, 1.329, 1.325$, and 1.318, respectively. The black curve in Fig. 4(d) shows the case when the channel is filled with DI water ($n = 1.318$). The resonance dips are found to shift toward longer wavelengths with increasing the value of n. These reflection spectra are measured, all at $\theta_i = 1^\circ$. To calculate the index sensitivity (S_b), the resonance wavelength of the device is plotted as a function of surrounding refractive index (Fig. 4(e)). The resonance wavelengths are found by fitting the data in the vicinity of minimal reflection using a 2nd order polynomial function. The slope of the linear fit in Fig. 4(e) is calculated as the index sensitivity $S_b = \Delta\lambda_r/\Delta n = 720$ nm/RIU.

3.3. Detection of breast cancer biomarker

The SNP-based biosensor can be utilized to detect biomolecules, such as DNA, protein, or small molecules, in real time. As an example, the device is used to quantify a well-established breast cancer biomarker, *ErbB2*. As a label-free technology, the SNP-based biosensor measures the refractive index change caused by the immobilization of

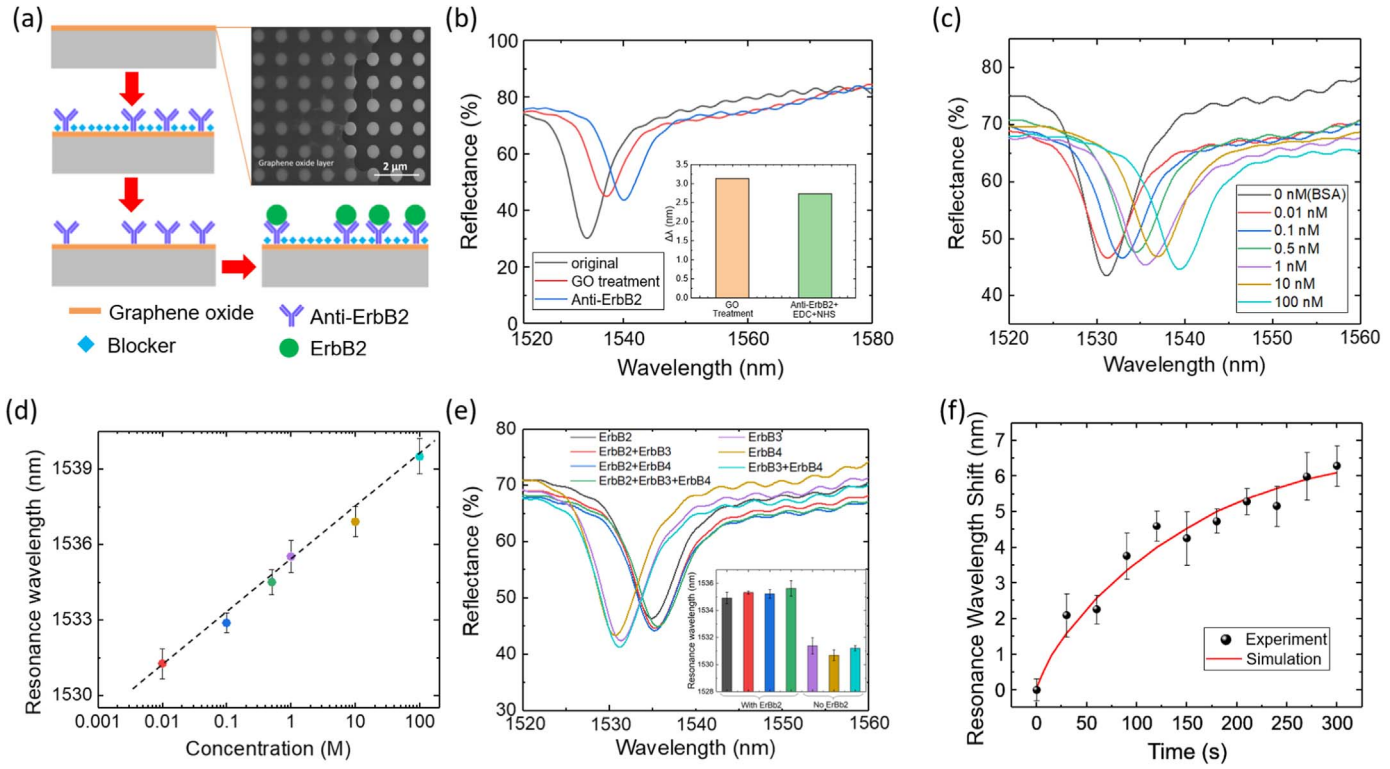

Fig. 5. (a) Schematics of the label-free assay and SEM of the SNPs with (left half) and without (right half) the GO coating. (b) Reflection spectra of the bare sensor, GO layer, and anti-*ErbB2* antibody coating. Inset: $\Delta\lambda_r$ after each step of the surface functionalization. (c) Reflection spectra measured in the present of *ErbB2* at a series of concentrations ranging from 0.01 to 100 nM. (d) Dose response curve for the detection of *ErbB2* by plotting the resonance wavelength as a function of the *ErbB2* concentration. (e) Reflection spectra measured for seven different combinations of *ErbB2*, *ErbB3*, and *ErbB4* antigens. Inset: sensor outputs in the presence of interfering molecules. (f)Simulation (red) and experiment (black) results of the kinetic binding of *ErbB2* and anti-*ErbB2* antibody.

the *ErbB2* molecules. The target *ErbB2* molecules are captured by the anti-*ErbB2* antibodies on the sensor surface. The details of this label-free assay are described in the Experimental section. Fig. 5(a) summarizes the major assay steps, including subsequent deposition of GO, anti-*ErbB2* antibody, and blocker, and the detection of *ErbB2* antigen. The SEM image in Fig. 5(a) show the SNPs with and without the GO coating. The thickness of the GO layer is about 30 nm. Fig. 5(b) presents the measured reflection spectra of the device when the SNPs is bared (black), coated with a GO layer (red), and functionalized with anti-*ErbB2* molecules.

Fig. 5(c) shows the reflectance spectra recorded when the samples containing *ErbB2* are injected into the nanofluidic channel. The sample solution is prepared by dissolved *ErbB2* in a phosphate-buffered saline (PBS; pH = 7.4) solution at six concentrations (0.01 nM, 0.1 nM, 0.5 nM, 1 nM, 10 nM, and 100 nM). As the concentration of *ErbB2* increases, the resonance dip in the reflection spectrum red shifts to longer wavelengths. The total shift of the resonance wavelength is approximately 6 nm when the *ErbB2* concentration increases from 0.01 nM to 100 nM. The dose response for the detection of *ErbB2* biomarker is shown in Fig. 5(d). The experiment with a specific *ErbB2* concentration repeats five times and the error bars represent the standard deviation of resonance wavelength for each concentration. The sensitivity of optical sensors can be estimated using $S_s = \Delta\lambda_r / \Delta c$, where Δc is the corresponding concentration difference. The SNP-based biosensor exhibits a sensitivity of 2 nm/nM for *ErbB2*.

Table 1 compares the key performance of this biosensor with some recently reported label-free biosensors for the detection of *ErbB2*. With regards to the sensitivity, the SNP-based biosensor outperforms the reported ring resonator biosensor (S_s = 0.12 nm/nM) and distributed feedback grating ($S_s = 2 \times 10^{-3}$ nm/nM) biosensor (Gohring et al., 2010; Retolaza et al., 2016). The limit of detection (LOD) of the SNP-based biosensor is found to be 0.7 ng mL^{-1} using the 3 *s* criterion (expressed in concentration units), where *s* represents the standard deviation of five-time measurements for the PBS solution. Compared to the other two optical biosensors, the SNP-based biosensor provides a lower LOD. In addition to the high refractive index sensitivity of the metasurface, the lateral flow-through design contributes significantly to the increased sensitivity and the lowered LOD by offering a useful

Table 1
Performance comparison of the lateral flow-through biosensor with other devices for the detection of *ErbB2*.

Device	Detection type/mode	Sensitivity	Detection range (nM)	Limit of detection (ng mL^{-1})	Ref.
Optofluidic silicon metasurface	Guided mode resonance	2 nm nM$^{-1/}$	0.01 – 10	0.7	This work
Optofluidic ring resonator	Whispering gallery mode	0.12 nm nM$^{-1/}$	0.14 – 3.45	13	(Gohring et al., 2010)
1D distributed feedback grating	1st-order diffraction mode	2×10^{-3} nm nM^{-1}	0.028 – 138	14	(Retolaza et al., 2016)
Hydrazine-Au nanoparticle-aptamer bioconjugate	Electrochemical	15×10^{-3} μA nM^{-1}	1×10^{-6} – 1.381	37	(Zhu et al., 2013b)
Sandwich magnetoimmunosensor	Electrochemical	1.4×10^{-4} μA nM^{-1}	1.4×10^{-3}– 0.4	0.026	(Eletxigerra et al., 2015)
Capacitance based aptasensor	Electrochemical	1.7×10^{-3} pF nM^{-1}	2.7 x10^{-3} – 2.7 × 10^{-2}	0.2	(Qureshi et al., 2015)

platform for realizing the syngeneic interaction between minute amounts of *ErbB2* proteins available in the sample and the capture molecules on the surface of SNPs. Although some of the reported electrochemical biosensors exhibit lower LOD values, our device presents a wider dynamic range.

To study the selectivity of the label-free biomarker detection assay, samples containing *ErbB2*, *ErbB3*, and *ErbB4* antigens were measured using the anti-*ErbB2* antibody-coated metasurface. These antigens belong to the *ErbB* receptor tyrosine kinase family, but the *ErbB3* and *ErbB4* antigens are nonspecific to the anti-*ErbB2* antibody (Ali et al., 2016b). Fig. 5(e) shows the measured reflection spectra of seven samples with different combinations of *ErbB2*, *ErbB3,* and *ErbB4* antigens (1 nM). The inset of Fig. 5(e) summarizes the resonance wavelength measured for these samples. The samples with the *ErbB2* antigen and interfering molecules result in a resonance wavelength shift of 6 nm. In contrast, the samples without *ErbB2* molecules show very small shift (< 1 nm) of the resonance wavelength. The results indicate that the SNP-based biosensor is selective to the target *ErbB2* antigen when the SNPs is functionalized using the anti-*ErbB2* antibody. As a label-free detection method, the biosensor can monitor the analyte-ligand binding process in real time. In this experiment, the reflection spectra were recorded when the *ErbB2* bound to the *ErbB2* antibody-coated sensor surface. Fig. 5(f) shows the temporal change of the resonance wavelength when the *ErbB2* sample (0.01 nM) passes through at a flow rate of 0.3 μL/min. The simulated and experimental results for *ErbB2* and anti-*ErbB2* binding are compared in Fig. 5(f). The error bars show the standard deviation of resonance wavelength shift for three replicated tests. The simulation of the binding process is performed using a finite element method (FEM) model that includes the fluid dynamics of the sample inside the nanofluidic channel, the diffusion of analyte from the solution to the sensor surface, and the surface reaction process. The details of the simulation are described in the Experiment section. The binding of the *ErbB2* to the surface results in an increase of λ_r around 6 nm.

4. Conclusions

In summary, this paper demonstrates a label-free, lateral flow-through biosensor that combines both biomolecule detection and sample delivery functions using the SOI-based metasurface. The SNPs provide numerous nanoscale flow channels to facilitate rapid delivery of analyte to the sensor surface. The device utilizes the GMR mode of the metasurface and operates in the telecom optical wavelength band. The linewidth of the resonance is tuned by changing the angle of incidence. The biosensor exhibits the refractive index sensitivity of 720 nm/RIU. The biosensor is studied for its ability to detect the *ErbB2* breast cancer biomarker. Because the SNP-based biosensor can be fabricated using the CMOS-compatible process, the device is amendable to integration with a wide variety of lab-on-a-chip components. We envision that the biosensor will enable rapid and quantitative analysis in point-of-care applications, such as disease diagnosis, drug test, and pathogen detection.

Acknowledgements

This work was supported by the United States National Science Foundation under Grant Nos. ECCS 17-11839 and ECCS 16-53673. The authors thank the Nano Fabrication Centre at the University of Minnesota for the support of device fabrication. YW acknowledges the Catron Center for Solar Energy Research for the Carton Graduate Fellowship.

Appendix A. Supporting information

Supplementary data associated with this article can be found in the online version at http://dx.doi.org/10.1016/j.bios.2018.02.038.

References

Ali, M.A., Mondal, K., Singh, C., Malhotra, B.D., Sharma, A., 2015. Nanoscale 7 (16), 7234–7245.
Ali, M.A., Hong, W., Oren, S., Wang, Q., Wang, Y., Jiang, H., Dong, L., 2016a. RSC Adv. 6 (71), 67184–67195.
Ali, M.A., Mondal, K., Jiao, Y.Y., Oren, S., Xu, Z., Sharma, A., Dong, L., 2016b. ACS Appl. Mater. Interfaces 8 (32), 20570–20582.
Ali, M.A., Singh, C., Srivastava, S., Admane, P., Agrawal, V.V., Sumana, G., John, R., Panda, A., Dong, L., Malhotra, B.D., 2017a. RSC Adv. 7 (57), 35982–35991.
Arnold, S., Khoshsima, M., Teraoka, I., Holler, S., Vollmer, F., 2003. Opt. Lett. 28 (4), 272–274.
Bergwerff, A.A., Van Knapen, F., 2006. J. AOAC Int. 89 (3), 826–831.
Brolo, A.G., Gordon, R., Leathem, B., Kavanagh, K.L., 2004. Langmuir 20 (12), 4813–4815.
Celebrano, M., Wu, X., Baselli, M., Grossmann, S., Biagioni, P., Locatelli, A., De Angelis, C., Cerullo, G., Osellame, R., Hecht, B., Duo, L., Ciccacci, F., Finazzi, M., 2015. Nat. Nanotechnol. 10 (5), 412–417.
Cetin, A.E., Coskun, A.F., Galarreta, B.C., Huang, M., Herman, D., Ozcan, A., Altug, H., 2014. Light-Sci. Appl. 3.
Chang-Hasnain, C.J., Yang, W., 2012. Adv. Opt. Photonics 4 (3), 379–440.
Cheung, S.T.S., Guan, B., Djordjevic, S.S., Okamoto, K., Yoo, S.J.B., 2012. Conference Laser. Electr.
Choi, C.J., Cunningham, B.T., 2006. Lab Chip 6 (10), 1373–1380.
Choi, C.J., Cunningham, B.T., 2007. Lab Chip 7 (5), 550–556.
Choi, C.J., Belobraydich, A.R., Chan, L.L., Mathias, P.C., Cunningham, B.T., 2010a. Anal. Biochem. 405 (1), 1–10.
Choi, C.J., Xu, Z., Wu, H.Y., Liu, G.L., Cunningham, B.T., 2010b. Nanotechnology 21, 41.
Cunningham, B.T., Li, P., Schulz, S., Lin, B., Baird, C., Gerstenmaier, J., Genick, C., Wang, F., Fine, E., Laing, L., 2004. J. Biomol. Screen 9 (6), 481–490.
Diaz-Diestra, D., Thapa, B., Beltran-Huarac, J., Weiner, B.R., Morell, G., 2017. Biosens. Bioelectron. 87, 693–700.
Eftekhari, F., Escobedo, C., Ferreira, J., Duan, X., Girotto, E.M., Brolo, A.G., Gordon, R., Sinton, D., 2009. Anal. Chem. 81 (11), 4308–4311.
Eletxigerra, U., Martinez-Perdiguero, J., Merino, S., Barderas, R., Torrente-Rodriguez, R.M., Villaionga, R., Pingarron, J.M., Carnpuzano, S., 2015. Biosens. Bioelectron. 70, 34–41.
Escobedo, C., Brolo, A.G., Gordon, R., Sinton, D., 2010. Anal. Chem. 82 (24), 10015–10020.
Fan, X., White, I.M., Shopova, S.I., Zhu, H., Suter, J.D., Sun, Y., 2008. Anal. Chim. Acta 620 (1–2), 8–26.
Fang, W., Huang, Y., Duan, X., Liu, K., Fei, J., Ren, X., 2016. Chin. Phys. B 25, 11.
Ferrara, J., Yang, W., Zhu, L., Qiao, P., Chang-Hasnain, C.J., 2015. Opt. Express 23 (3), 2512–2523.
Fivash, M., Towler, E.M., Fisher, R.J., 1998. Curr. Opin. Biotechnol. 9 (1), 97–101.
Gohring, J.T., Dale, P.S., Fan, X., 2010. Sens. Actuators B-Chem. 146 (1), 226–230.
Heeres, J.T., Kim, S.H., Leslie, B.J., Lidstone, E.A., Cunningham, B.T., Hergenrother, P.J., 2009. J. Am. Chem. Soc. 131 (51), 18202 (+).
Im, H., Shao, H., Park, Y.I., Peterson, V.M., Castro, C.M., Weissleder, R., Lee, H., 2014. Nat. Biotechnol. 32 (5) (490-U219).
Lindquist, N.C., Lesuffleur, A., Im, H., Oh, S.H., 2009. Lab Chip 9 (3), 382–387.
Liu, L., Xu, Z., Dong, L., Lu, M., 2014. Opt. Lett. 39 (9), 2751–2754.
de Mol, N.J., 2012. Methods Mol. Biol. 800, 33–53.
McDonnell, J.M., 2001. Curr. Opin. Chem. Biol. 5 (5), 572–577.
Navratilova, I., Hopkins, A.L., 2011. Future Med. Chem. 3 (14), 1809–1820.
Qureshi, A., Gurbuz, Y., Niazi, J.H., 2015. Sens. Actuators B-Chem. 220, 1145–1151.
Retolaza, A., Martinez-Perdiguero, J., Merino, S., Morales-Vidal, M., Boj, P.G., Quintana, J.A., Villalvilla, J.M., Diaz-Garcia, M.A., 2016. Sens. Actuaors B-Chem. 223, 261–265.
Rich, R.L., Myszka, D.G., 2003. Trends Microbiol. 11 (3), 124–133.
Salafsky, J.S., 2006. J. Chem. Phys. 125 (7).
Sinton, D., Gordon, R., Brolo, A.G., 2008. Microfluid. Nanofluid. 4 (1–2), 107–116.
Sridharamurthy, S.S., Dong, L., Jiang, H.R., 2007. Meas. Sci. Technol. 18 (1), 201–207.
Sun, M., Sun, T., Liu, Y., Zhu, L., Liu, F., Huang, Y., Chang-Hasnain, V., 2016a. Proc. SPIE 9757, 97570Q–97571Q.
Sun, T., Kan, S., Marriott, G., Chang-Hasnain, C., 2016b. Sci. Rep.- U.K. 6.
Sun, Y.Z., Fan, X.D., 2011. Anal. Bioanal. Chem. 399 (1), 205–211.
Taillaert, D., Van Laere, F., Ayre, M., Bogaerts, W., Van Thourhout, D., Bienstman, P., Baets, R., 2006. Jpn. J. Appl. Phys. 1 (8a), 6071–6077 (45).
Thillaivinayagalingam, P., Gommeaux, J., McLoughlin, M., Collins, D., Newcombe, A.R., 2010. J. Chromatogr. B 878 (2), 149–153.
Van Laere, F., Claes, T., Schrauwen, J., Scheerlinck, S., Bogaerts, W., Taillaert, D., O'Faolain, L., Van Thourhout, D., Baets, R., 2007. IEEE Photon. Technol. Lett. 19 (21–24), 1919–1921.
Vollmer, F., Arnold, S., 2008. Nat. Methods 5 (7), 591–596.
Wang, Y., Kar, A., Paterson, A., Kourentzi, K., Le, H., Ruchhoeft, P., Wilson, R., Bao, J., 2014. ACS Photonics 1 (3), 241–245.
Wang, Y., Dong, L., Lu, M., 2016a. Conference Laser. Electr.
Wang, Y., Song, J., Dong, L., Lu, M., 2016b. J. Opt. Soc. Am. B 33 (12), 2472–2479.
White, I.M., Oveys, H., Fan, X., 2006. Opt. Lett. 31 (9), 1319–1321.
Wu, H.Y., Choi, C.J., Cunningham, B.T., 2012. Conference Laser. Electr.
Xue, T., Cui, X., Guan, W., Wang, Q., Liu, C., Wang, H., Qi, K., Singh, D.J., Zheng, W., 2014a. Biosens. Bioelectron. 58, 374–379.
Xue, T., Wang, Z., Guan, W., Hou, C., Shi, Z., Zheng, W., Cui, X., 2014b. RSC Adv. 4 (92), 50789–50794.
Yanik, A.A., Huang, M., Artar, A., Chang, T.Y., Altug, H., 2010. Appl. Phys. Lett. 96, 2.
Yin, D., Schmidt, H., Barber, J.P., Hawkins, A.R., 2004. Opt. Express 12 (12), 2710–2715.
Zhang, W., Ganesh, N., Block, I.D., Cunningham, B.T., 2008. Sens. Actuators B-Chem. 131 (1), 279–284.
Zhu, L., Yang, W., Chang-Hasnain, C.J., 2013a. Proc. SPIE 8633.
Zhu, L., Kapraun, J., Ferrara, J., Chang-Hasnain, C.J., 2015. Optica 2 (3), 255–258.
Zhu, Y., Chandra, P., Shim, Y.B., 2013b. Anal. Chem. 85 (2), 1058–1064.